IEEE Photonics Journal
An IEEE Photonics Society Publication

Open Access

Manufacturing Tolerance Analysis of an MMI-Based 90° Optical Hybrid for InP Integrated Coherent Receivers

Volume 5, Number 2, April 2013

J. S. Fandiño
P. Muñoz, Member, IEEE

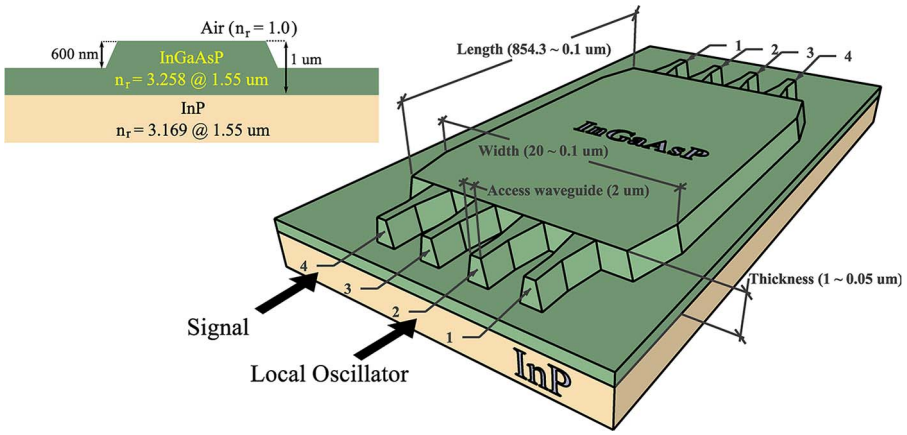

DOI: 10.1109/JPHOT.2013.2247994
1943-0655/$31.00 ©2013 IEEE

IEEE photonics SOCIETY

IEEE

Manufacturing Tolerance Analysis of an MMI-Based 90° Optical Hybrid for InP Integrated Coherent Receivers

J. S. Fandiño and P. Muñoz, *Member, IEEE*

Optical and Quantum Communications Group, ITEAM Research Institute, Universidad Politécnica de Valencia, Camino de Vera s/n, 46022 Valencia, Spain

DOI: 10.1109/JPHOT.2013.2247994
1943-0655/$31.00 ©2013 IEEE

Manuscript received January 21, 2013; revised February 12, 2013; accepted February 12, 2013. Date of publication February 20, 2013; date of current version March 8, 2013. This work was supported in part by the Spanish MICINN Project TEC2010-21337, acronym ATOMIC, and in part by projects FEDER UPVOV10-3E-492 and UPVOV08-3E-008. The work of J. S. Fandiño was supported by Grant FPU-2010 (ref: AP2010-1595). Corresponding author: J. S. Fandiño (e-mail: jasanfan@upvnet.upv.es).

Abstract: A numerical study of the impact that manufacturing tolerances have on the performance of an InP 4×4 MMI working as a 90° optical hybrid is presented, including simultaneous variations of width, thickness, and refractive index over the C and L bands. Simulation results for different figures of merit, such as optical common-mode rejection ratios (CMRRs) and phase errors, are provided for both nominal and worst case scenarios. Additionally, system simulations are performed to compute imbalance-induced power penalty. Our results indicate that the combined effect of realistic foundry tolerances on device performance is significant. In particular, a fourfold reduction is predicted between nominal ($\simeq$40 nm) and worst cases ($\simeq$10 nm) when optical CMRRs and phase errors are compared against Optical Internetworking Forum specifications. By contrast, a much greater bandwidth is expected at the system level ($\geq$ 40 nm) if a power penalty of less than 1 dB ($@\text{BER} = 10^{-3}$) is to be allowed. In fact, worst case power penalties lower than 0.25 dB are predicted over the full C band, which further proves the great potential of integrated 4×4 MMIs as wide-bandwidth devices for mass production of coherent receivers using state-of-the-art integration technologies.

Index Terms: Coherent optical communications, integrated optics, 90° optical hybrid, multimode interference coupler, digital coherent receivers.

1. Introduction

During the past few years, DSP-based coherent optical communications have emerged as the most promising transmission technology for keeping up with the exploding growth in global data traffic [1]. Thanks to the advancement of both high-performance photonic integrated circuits (PICs) and ultra-high-speed electronics, real-time coherent optical super channels operating at aggregate speeds of up to 500 Gb/s have become a commercial reality [2], [3]. On one side, PICs have provided a cost-effective mean of realizing reliable transmitter and receiver optical front ends for advanced modulation formats, whereas state-of-the-art high-bandwidth ADCs and DSPs have allowed for reconstruction of the transmitted optical field.

90° optical hybrids are undoubtedly one of the key building blocks that comprise an integrated coherent receiver. Although several configurations for these devices have been proposed and demonstrated so far [4], [5], MMI-based 90° optical hybrids have recently attracted considerable research attention since they offer superior performance in terms of size, operation bandwidth, and

polarization independence. By means of a careful design, devices operating over the full C band while keeping low common-mode rejection ratios (CMRRs ~ -20 dBe) and phase errors ($\Delta\phi_{err} \sim \pm 5^{\circ}$) have been demonstrated, both in InP and SOI technologies [5]–[13]. As a result, integrated coherent receiver modules with MMI-based 90° optical hybrids have already reached the commercial stage [7], paving the way for future high-performance PICs in next generation coherent optical communication systems.

However, several factors can significantly degrade the ideal quadrature phase response of the designed 90° optical hybrid, such as deviations in cross section geometry caused by lithography and etching. Although manufacturing deviations are of fundamental importance in final hybrid's performance, there has been little research on understanding the combined impact of all of them at the same time or how they ultimately affect overall system penalty. On one hand, previous numerical estimations of MMI's bandwidth have considered nominal design values while sweeping operation wavelength [8], [12]. At most, 1-D sweeps at a single wavelength of some geometrical features have been performed in 2×2 [14] and 4×4 MMIs [13]. On the other hand, previous works on imbalance compensation algorithms have considered generic imbalance values without resorting to either numerical results or experimental data from manufactured devices [15], [16]. In this paper, we aim to bridge the gap between these two abstraction levels. In order to do so, we perform a systematic numerical evaluation of the impact that several, simultaneous manufacturing deviations have on both the optical and system level performance of an integrated, 4×4 MMI-based 90° optical hybrid, which is designed using an available generic InP platform. These include width and thickness variations, as well as changes in waveguide's core refractive index.

This paper is organized as follows. In Section 2, the optical device level multi-sweep simulation procedure is described, where measured fabrication tolerances provided by the foundry are used to numerically determine the transmission response of the hybrid along the C and L bands. We provide results for different figures of merit of an optical hybrid, such as CMRRs, phase errors, and excess losses, showing the significant impact that these deviations can have on device performance. Results are then exported in Section 3 to a simplified system model, so as to get a deeper understanding of how imbalance ultimately transforms into power penalty. As we shall see, optically defined CMRRs and phase errors do not provide an accurate estimation of operation bandwidth if power penalty is of major importance. In fact, a $\simeq$40-nm operation bandwidth (1530–1570 nm) is demonstrated for a penalty of less than 1 dB ($@\text{BER} = 10^{-3}$) in the worst case conditions, as compared with the 10-nm bandwidth (1540–1550 nm) obtained in the optical domain. Conclusions are shown in Section 4.

2. Optical Device Level Simulation

First, commercially available software tools (FieldDesigner and OptoDesigner, PhoeniX Software) were employed to design a 4×4 MMI working as a 90° optical hybrid. At this stage, both MMI's width and etch depth need to be carefully chosen since there is an inherent tradeoff between device footprint and operation bandwidth. If one seeks to achieve high operation bandwidth, the propagation constants of the different modes in the multimode section should ideally follow a quadratic relationship [6]. In practice, deeply etched structures considerably deviate from this ideal behavior, specially when higher order modes are considered. By contrast, the use of shallow-etch waveguides implies larger separation gaps between access ports in order to avoid input/output power coupling, which, in turn, yields long devices. After some preliminary simulations, an intermediate rib height of 0.6 μm proved as an appropriate balance. The final device size is 20 μm in width and 854.3 μm in length, excluding input and output waveguides, and was optimized for 1550 nm as nominal wavelength. The rib waveguides are comprised of an InGaAsP core ($\text{n} = 3.258 @ \lambda = 1.55$ μm) over an InP substrate ($\text{n} = 3.169 @ \lambda = 1.55$ μm), with an etch depth measured from the top of the core of 600 nm. No cladding is employed. A 3-D representation of the simulated device can be seen in Fig. 1, along with a cross-section view of the waveguides. It summarizes both material and geometrical parameters, such as final design values and manufacturing tolerances. The latter include variations in waveguides' width and length (± 0.1 μm), as well as absolute

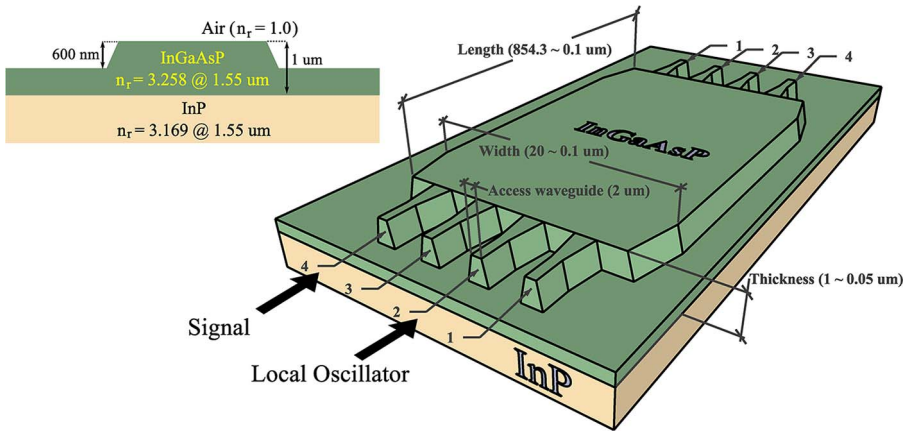

Fig. 1. Conceptual representation of the InP rib-waveguide-based 4 × 4 MMI. Main physical parameters are shown, along with their nominal design values and foundry manufacturing tolerances.

changes in InGaAsP refractive index (±0.004 over the full wavelength range) and core thickness ($\pm 0.05\ \mu$m).

The simulation procedure can be described as follows. An interval around each nominal design value is considered for all parameters under analysis (width, thickness, and refractive index). Length deviations were excluded to reduce simulation time, as they have negligible impact on device performance [17]. Each interval is then discretized into 3 data points, which include the nominal as well as the two worst case values. Afterwards, these values are accordingly combined to form all possible ($3^3 = 27$) combinations [see Fig. 2(a)]. The wavelength is varied in steps of 2.5 nm over the C and L bands (1530–1625 nm), where we also account for refractive index wavelength dependence of materials (InP and InGaAsP). For every new wavelength point, one simulation cycle is run. Each simulation cycle includes 27 film mode matching (FMM) mode-solving calculations of the new MMI cross section; 3-D to 2-D reduction using an optimized effective index method (EIM) approximation; and optical field propagation by means of 2-D beam propagation (2-D-BPM), in order to compute hybrid's field transmission coefficients for the two possible input ports (signal and LO). These coefficients are automatically computed by the simulation software using mode overlap integrals between the simulated field in the multimode waveguide and the fundamental mode of the output waveguides. Their squared magnitude gives the transmitted optical power, whereas their phase is the relative phase shift between input and output ports. All other parameters, such as input/output waveguides' width and position, are kept fixed. Note that the tolerances of our process are very small relative to nominal design values. For example, MMI's width (which is the most critical parameter) has a relative variation of less than 0.5%. Thus, it is expected that any possible process variation contained within the aforementioned intervals will lead to smaller changes in MMI's imaging length. The lower the resulting length deviation, the lower power imbalance, excess losses, and phase errors. As a consequence, only the upper and lower bounds of these intervals were considered to reduce simulation time and assumed to represent worst case conditions, which is consistent with previous simulation work on MMI-based 90° optical hybrids [14].

Since our tolerance analysis expands in a 4-D space, a versatile visualization technique called *dimensional stacking* was employed to represent results and gain some preliminary insight into possible relationships among parameters and figures of merit before further post-processing [18]. This concept is illustrated in Fig. 2(a). The main idea behind this technique is to recursively represent N-dimensional results by plotting a given pair of dimensions within blocks, which correspond to points of other pairs of dimensions. In our case, blocks of 3 × 3 pixels (black and white colored) separated by soft grey lines correspond to simultaneous variations of width and thickness, where refractive index and wavelength are kept constant. Adjacent 3 × 3 blocks, which are separated by dark grey lines, correspond to width and thickness variations for a different refractive index and wavelength (vertical and horizontal directions, respectively). Note that parameter values increase

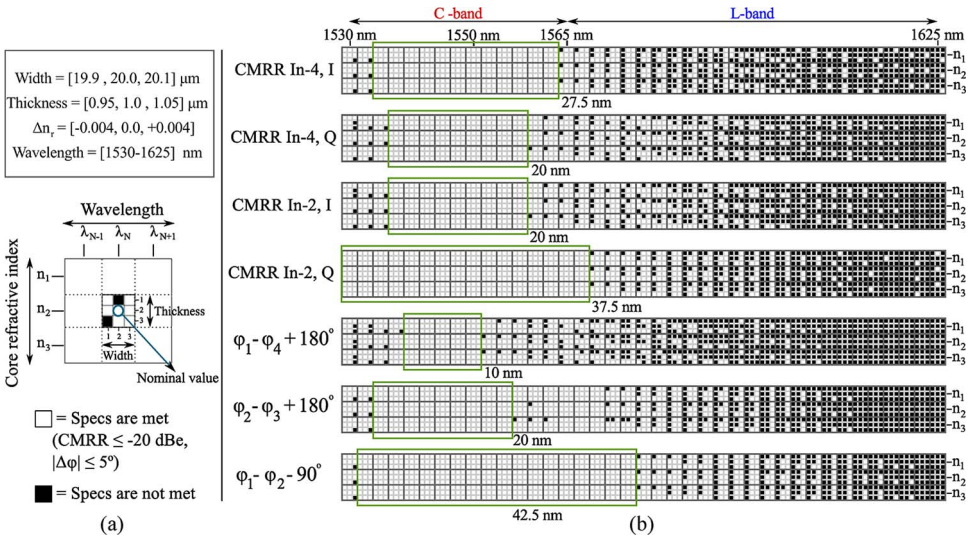

Fig. 2. (a) Sweep parameter values and conceptual representation of the *dimensional stacking* visualization technique. (b) Representation of the main figures of merit [6], compared against OIF specifications. Bandwidths over which these specifications are met for all possible manufacturing deviations are enclosed by dark green lines.

from left to right and from top to bottom. This means that, for example, pixels in the center of each 3 $\times$ 3 block represent nominal design values of width and thickness, whereas the ones in the upper left corner represent the case in which both width and thickness are reduced with respect the their nominal value (19.9 μm and 0.95 μm, respectively).

Results are shown in Fig. 2(b), where hybrid's figures of merit (CMRRs and phase errors) are plotted using the aforementioned visualization technique. The CMRRs quantify the optical power splitting uniformity across output ports when the hybrid is accessed by a given input port (either signal or LO), whereas the phase errors measure the deviation of the output signals with respect to the ideal phase response of a perfect 4 $\times$ 4 MMI. The mathematical definition of these quantities can be readily found in [6] and [19]. The only difference is that our phases are measured in an interval between -180° and $+180^\circ$; thus, two of our definitions for the phase errors differ by a $+$ symbol from those of [6] (in particular, $\phi_2 - \phi_3 + 180^\circ$ and $\phi_1 - \phi_4 + 180^\circ$). In order to reduce the vast amount of information, pixels are simply colored white when values go over a certain threshold, and black otherwise. These thresholds were set to match those specified by the Optical Internetworking Forum (OIF) implementation agreement [19], which are normally used as a reference in the literature [6], [9], [11]. Even if this threshold operation prevents us from looking at the actual values, a lot of information can be gained at first glance. First, it can be seen that there is a small interval of wavelengths near 1550 nm (target design), where the hybrid meets OIF specifications for all figures of merit, independently of tolerance deviations. Thus, blocks are fully white colored, indicating that specifications are satisfied in all cases. As the wavelength is reduced, some black pixels start to show up on the lower right corners. This indicates that reducing wavelength while increasing both waveguide width and guiding layer thickness further confines propagation modes inside the multimode waveguide, which makes optimal length considerably deviate from its nominal design. If the wavelength is increased toward the L band, the opposite effect occurs. This is in agreement with MMI theory since imaging length gets bigger/lower as the mode confinement increases/decreases [20]. Finally, notice how the black and white patterns in the vertical columns of 3 $\times$ 3 blocks are almost identical when the refractive index is varied. Hence, refractive index variations have negligible impact on device performance, which is mainly determined by width and thickness tolerances.

Further post-processing of the aforementioned results leads naturally to Figs. 3 and 4, where figures of merit across the C and L bands are shown both for ideal and worst cases. Note that, here, *worst case* refers to the worst performing device evaluated at each wavelength. This is, at each

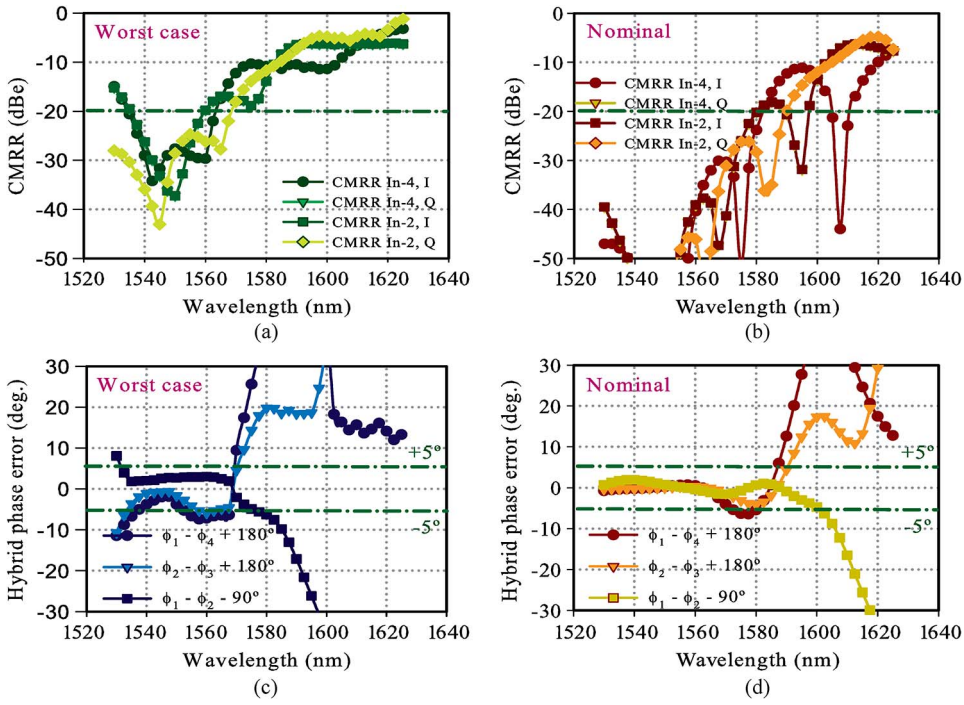

Fig. 3. Simulated optical CMRRs (a-b) and phase errors (c-d) for both nominal and worst cases over the C and L bands. Maximum values permitted by OIF's standard are shown as dark green dashed lines.

wavelength, every figure of merit is evaluated for all possible combinations of cross section parameters, and the worst value is chosen each time [see Fig. 2(b)]. Thus, it serves as an upper bound below which all possible hybrids will be located after manufacturing, even though single devices may show significantly better performance. In this way, the nominal design can be compared against an aggregate combination of manufacturing deviations in a real scenario, and it could even be used as a worst case value in the data sheet of the device if it were to undergo mass production. As it can be seen in Fig. 3, taking tolerances into account yields a significant difference in operating bandwidth. If OIF specifications are to be strictly observed (CMRR ≤ -20 dBe, $\Delta\phi_{\text{err}} \leq \pm 5°$), only 10 nm (1540–1550 nm) are achieved in the worst case. On the contrary, up to 40 nm (1530–1570 nm) are guaranteed for the nominal design, similar to previously reported experimental results using the same technology [10], [21]. Thus, target specifications are only to be met by all manufactured devices over a 10-nm bandwidth in a real mass production environment, where random deviations across the wafer are unavoidable. This highlights the importance of taking tolerances into account when determining the performance of integrated optical devices via simulation. In both cases, note also that the hybrid considerably deviates from the expected behavior over the L band. This is caused by a lower number of modes propagating inside the MMI as the wavelength increases, resulting in poorer imaging and higher excess losses (see Fig. 4).

3. System Level Evaluation

Although optical CMRRs and phase errors are a useful way of quantifying the performance of manufactured 90° optical hybrids at a physical level, it is not clear though how these figures of merit ultimately translate into system performance. This is typically measured as a power penalty (for the same BER) with respect to an ideal situation where no such imbalance occurs, and it is to be minimized when designing digital communication systems. In this section, we proceed to compute the power penalty produced by the non-ideal optical hybrid simulated in Section 2, assuming that the system is corrupted only by additive white Gaussian noise (AWGN). This penalty is therefore the

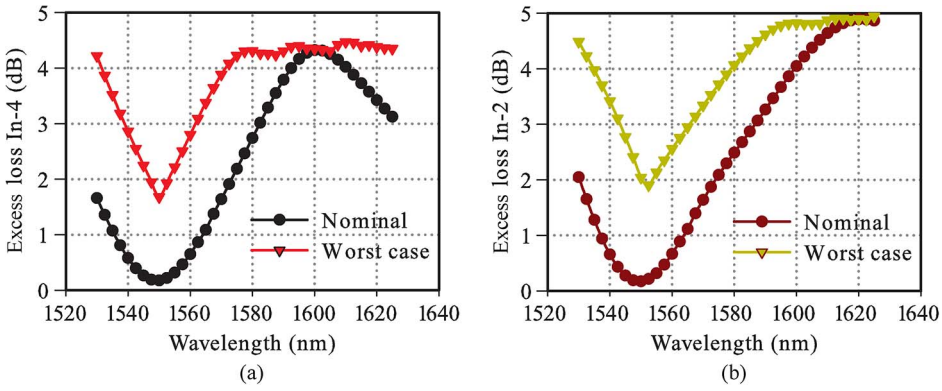

Fig. 4. Simulated excess losses for signal input port (a) and local oscillator (b) as a function of wavelength.

minimum one which could be theoretically achieved under the assumption of a system limited by ASE noise, if all other impairments were to be removed. ASE-limited operation, where the local oscillator (LO)-ASE beating noise is dominant over all the other noise components, is a common and reasonable assumption in long-haul, amplified links [22]. Consequently, this penalty can be used by PIC designers to quantitatively assess the quality of their designs and their resilience to fabrication problems. Since BER is the main concern in coherent communication systems, it represents a fairer approach for estimating hybrid's operation bandwidth via simulation. Besides, notice that although several imbalance compensation algorithms have been proposed so far [15], [16], the goal of PIC designers is to maximize performance at the optical level. By designing low imbalance and highly resilient coherent transmitters and receivers, the computing effort wasted in compensating for these impairments could eventually be removed.

First, we shall show how the analytical BER of our ideal differentially encoded QPSK (DE-QPSK) system can be directly computed from optical parameters that can be easily measured using standard instrumentation, such as the optical signal-to-noise ratio (OSNR). Afterwards, we shall proceed to analytically and numerically investigate the effect that optical imbalance has in the electrical domain. Finally, the simulation procedure will be described, and results will be discussed and compared with those in Section 2.

A block diagram of our simplified system model is shown in Fig. 5. A single polarization, DE-QPSK modulated laser signal is sent through an ideal channel where additive, depolarized ASE noise due to amplification through the link is present. The optical fields of both signal and LO, assuming ideal monochromatic sources, can be described as [22]

$$\mathbf{E}_s(t) = \sqrt{P_s}\sum_k p(t - kT_s)\exp(j(\omega_s t + \phi_k))\mathbf{e}_s \tag{1}$$

$$\mathbf{E}_{lo}(t) = \sqrt{P_{lo}}\exp(j\omega_{lo} t)\mathbf{e}_{lo} \tag{2}$$

where T_s is the symbol period, $p(t)$ is a conveniently normalized pulse shape, ϕ_k is the modulated DE-QPSK phase at a given symbol interval, and ω_s and ω_{lo} are the optical angular frequencies of the signal and LO, respectively. Their CW optical powers are given by P_s and P_{lo}. 2-D complex vectors ($\mathbf{e}_s$ and $\mathbf{e}_{lo}$), also known as Jones vectors, are used to represent the state of polarization of the lasers with respect to an arbitrarily chosen orthogonal coordinate system. The additive, depolarized optical ASE noise present in the channel can in turn be described by [1]

$$\mathbf{n}(t) = n_{\parallel}(t)\mathbf{e}_{\parallel} + n_{\perp}(t)\mathbf{e}_{\perp} \tag{3}$$

being both $n_{\parallel}(t)$ and $n_{\perp}(t)$ uncorrelated, complex, zero-mean AWGN processes with a single-sided power spectral density given by $N_0/2$. Note that each polarization ($\mathbf{e}_{\parallel}$ and $\mathbf{e}_{\perp}$) carries half of the total

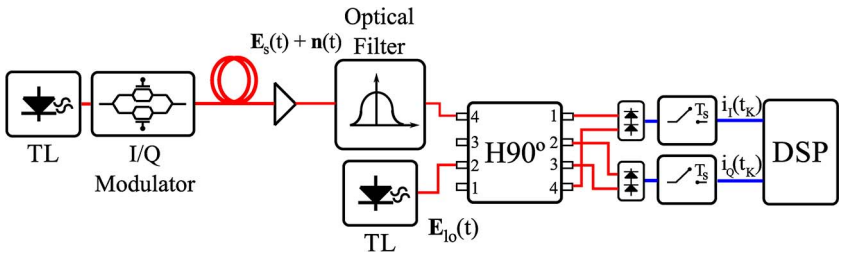

Fig. 5. Schematic representation of the simplified system model employed to evaluate hybrid-induced penalty.

single-sided power spectral density (N_0), which is the ASE power measured in an optical spectrum analyzer (OSA) divided by the instrument's resolution bandwidth.

After optical filtering by a nominal Gaussian filter, the LO and the signal are mixed in the 90° optical hybrid. Both LO and signal are assumed to be polarization aligned. Finally, one pair of balanced photodetectors and high-speed ADCs converts the optical signals into digital samples before DSP-based information recovery. Using well-known formulas for the photodetection process (see, for example, [23], p. 31), the approximated sampled I/Q photocurrents at the optimum sampling time $(t_k = kT_s)$ are given by

$$i_I(t_k) \simeq \frac{\eta q}{\hbar \omega_s} \sqrt{P_s P_{lo}} \Re\{\exp(j\phi_k)\} + n_I(t_k) \tag{4}$$

$$i_Q(t_k) \simeq \frac{\eta q}{\hbar \omega_s} \sqrt{P_s P_{lo}} \Im\{\exp(j\phi_k)\} + n_Q(t_k) \tag{5}$$

where $\Re\{\}$ and $\Im\{\}$ stand for the real and imaginary parts of a given complex number, η is the quantum efficiency of the balanced photodiodes, q is the electron charge, and $\hbar$ is the reduced Planck's constant. The noise terms, $n_I(t_k)$ and $n_Q(t_k)$, are random, uncorrelated Gaussian variables with variance

$$\sigma_I^2 = \sigma_Q^2 = \left(\frac{\eta q}{\hbar \omega_s}\right)^2 \frac{P_{lo} N_0 B_{eff}}{2}. \tag{6}$$

This variance depends on the effective noise bandwidth (B_{eff}) of the nominal Gaussian filter, which is related to its 3-dB bandwidth via a filter-shape dependent constant

$$B_{eff} = \frac{\sqrt{\pi} \Delta f_{3\,\mathrm{dB}}}{4\sqrt{\ln(2)}}. \tag{7}$$

Here, $\Delta f_{3\,\mathrm{dB}}$ is the full-width 3-dB bandwidth, and $\ln()$ stands for the natural logarithm function. In practice, the presence of multiple reconfigurable optical add/drop multiplexers (ROADMs) in the signal path imposes more stringent requirements on the optical filters. Their combined effect (coupled with individual wavelengths drifts) effectively *peels off* the bandwidth of the signal, which can be readily avoided by increasing the flatness of the pass-band. For 100-Gb/s channels, it has been estimated that up to a fourth-order Gaussian filter would be required [24]. In our case, the nominal Gaussian filter is assumed not to affect the signal bandwidth, but is employed to reject out-of-band ASE noise. A lower value of B_{eff} implies that less noise is coupled into the system for a fixed $\Delta f_{3\,\mathrm{dB}}$. The ratio between the effective noise bandwidth of a nominal Gaussian and that of a fourth-order Gaussian (for any $\Delta f_{3\,\mathrm{dB}}$) is approximately 1.08. This means that, by employing a fourth-order Gaussian filter instead of a nominal one, the measured OSNR is marginally increased by about 0.33 dB. Thus, our approximation is well justified and ultimately serves as a worst case estimation.

The differentially encoded data is finally recovered using a hard-decision, differential decoding scheme, where decisions on the sampled phases are taken prior to differential decoding of detected

symbols [25]. Gray coding of the differentially modulated symbols is also assumed. The analytical BER formula for such an ideal receiver was recently derived by Simon [26]

$$P_b|_{\text{DE-QPSK}} = \text{erfc}\left(\sqrt{\frac{E_s}{2N_0'}}\right) - \frac{1}{2}\text{erfc}^2\left(\sqrt{\frac{E_s}{2N_0'}}\right) \tag{8}$$

where erfc() stands for the complementary error function, and E_s/N_0' is the symbol energy-to-noise ratio. E_s can be computed as the average squared magnitude of the received constellation points on the complex plane, whereas N_0' is defined as the sum of the variances of both the I and Q AWGN noises. Note the slight change in notation to distinguish this quantity from the already defined single-sided power spectral density of the ASE noise (N_0). In this particular case

$$E_s = \left(\frac{\eta q}{\hbar\omega_s}\right)^2 P_s P_{lo} \tag{9}$$

$$N_0' = \sigma_I^2 + \sigma_Q^2 = \left(\frac{\eta q}{\hbar\omega_s}\right)^2 P_{lo} N_0 B_{eff} \tag{10}$$

which yields

$$\frac{E_s}{N_0'} = \frac{P_s}{N_0 B_{eff}}. \tag{11}$$

By noting that the OSNR at a certain resolution bandwidth (B_{res}) is defined as $\text{OSNR} = P_s/(N_0 B_{res})$ and by substituting (7) into (11), we finally get

$$\frac{E_s}{N_0'} = \frac{4\sqrt{\ln(2)}B_{res}\text{OSNR}}{\sqrt{\pi}\Delta f_{3\text{ dB}}}. \tag{12}$$

Equation (12) is useful because it allows us to relate easily measurable optical parameters with the final signal energy-to-noise ratio (E_s/N_0'), which determines system BER through (8). Note also that, under the assumption of ASE-limited operation, the power from the LO has no effect on the BER since it amplifies both signal and noise equally during photodetection.

Now, let us show what happens when a non-ideal hybrid is considered. In this case, the ideal field transmission matrix of the hybrid (see, for example, [1], p. 84) has to be modified accordingly with a new set of coefficients. This new matrix can be expressed in its most general form as

$$\mathbf{H} = \begin{bmatrix} \alpha_1 & \alpha_2 \\ \alpha_3 & \alpha_4 \\ \alpha_5 & \alpha_6 \\ \alpha_7 & \alpha_8 \end{bmatrix} \tag{13}$$

where α_i are complex numbers which represent hybrid's field transmission coefficients, exactly as those directly provided by the software in Section 2. The first and second columns contain the coefficients at the 4 output ports (1–4, from top to bottom) when the hybrid is accessed by the LO and signal ports (2 and 4, from bottom to top), respectively (see Fig. 5). This is

$$\begin{bmatrix} \mathbf{E}_{\text{out}_1} \\ \mathbf{E}_{\text{out}_2} \\ \mathbf{E}_{\text{out}_3} \\ \mathbf{E}_{\text{out}_4} \end{bmatrix} = \begin{bmatrix} \alpha_1 & \alpha_2 \\ \alpha_3 & \alpha_4 \\ \alpha_5 & \alpha_6 \\ \alpha_7 & \alpha_8 \end{bmatrix} \begin{bmatrix} \mathbf{E}_s \\ \mathbf{E}_{lo} \end{bmatrix}. \tag{14}$$

As a result, the beating currents in (4) and (5) no longer hold. After some straightforward algebraic manipulation, it can be shown that the new beat currents ($i_I'(t_k)$ and $i_Q'(t_k)$) can be simply

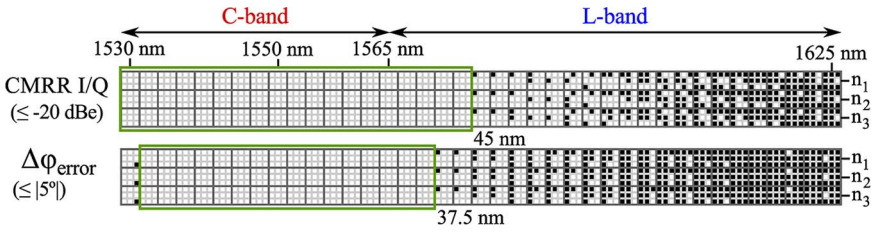

Fig. 6. *Dimensional stacking* representation of the simulated electrical CMRR and phase error along the C and L bands, as defined in (20) and (21). Bandwidths over which these specifications are met for all possible manufacturing deviations are enclosed by dark green lines.

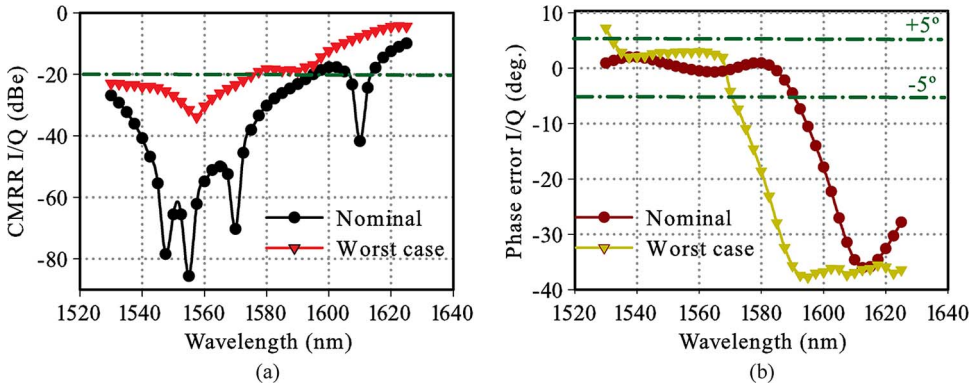

Fig. 7. Simulated electrical CMRR (a) and phase error (b) along the C and L bands. Both nominal and worst cases are shown.

related to the ideal ones in (4) and (5) by a 2×2 real-valued matrix (Σ)

$$\begin{bmatrix} i_I'(t_k) \\ i_Q'(t_k) \end{bmatrix} = \Sigma \begin{bmatrix} i_I(t_k) \\ i_Q(t_k) \end{bmatrix} = \begin{bmatrix} \sigma_1 & \sigma_2 \\ \sigma_3 & \sigma_4 \end{bmatrix} \begin{bmatrix} i_I(t_k) \\ i_Q(t_k) \end{bmatrix} \tag{15}$$

whose coefficients (σ_i) can be directly computed from those of (14) employing the following relations:

$$\sigma_1 = 2\left(\Re\left\{\alpha_1\alpha_2^* - \alpha_7\alpha_8^*\right\}\right) \tag{16}$$

$$\sigma_2 = 2\left(\Im\left\{\alpha_7\alpha_8^* - \alpha_1\alpha_2^*\right\}\right) \tag{17}$$

$$\sigma_3 = 2\left(\Re\left\{\alpha_3\alpha_4^* - \alpha_5\alpha_6^*\right\}\right) \tag{18}$$

$$\sigma_4 = 2\left(\Im\left\{\alpha_5\alpha_6^* - \alpha_3\alpha_4^*\right\}\right). \tag{19}$$

Note that, for an ideal hybrid, Σ results in the identity matrix (I); thus, $i_I'(t_k) = i_I(t_k)$, and $i_Q'(t_k) = i_Q(t_k)$. In practice, there is always a certain amount of optical imbalance, which translates into correlation between I and Q channels. This implies a distortion of the received constellation shape, as well as the presence of correlated AWGN noise, leading to an increase in system BER. However, by taking a closer look at equations (16)–(19), it can be seen that deviations both in power and phase at different ports of the hybrid may cancel each other after photodetection. For example, $|\alpha_1|$ (signal) could decrease a little, whereas $|\alpha_2|$ (LO) could increase inversely, leaving their product unchanged. As a consequence, the presence of optical imbalance does not necessarily translate into electrical imbalance, which is directly related to system performance. Thus, a more convenient and natural way of quantifying performance is to use the CMRR and phase error

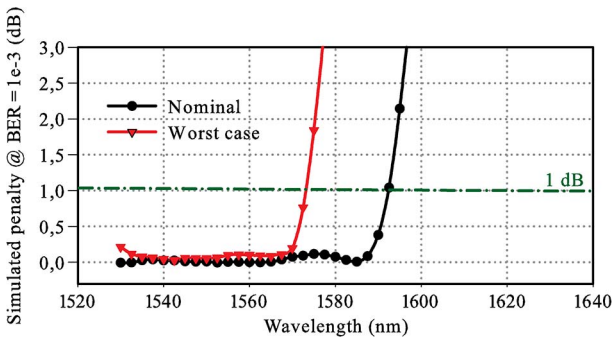

Fig. 8. Simulated penalty $(@\text{BER} = 10^{-3})$ with respect to an ideal, ASE-limited system.

between electrical I and Q channels, rather than CMRRs and phase errors in the optical domain. These can be defined as

$$\text{CMRR}_{I/Q} = 20\log\left(\frac{\left|\left[\sigma_1^2+\sigma_3^2\right]^{\frac{1}{2}}-\left[\sigma_2^2+\sigma_4^2\right]^{\frac{1}{2}}\right|}{\left[\sigma_1^2+\sigma_3^2\right]^{\frac{1}{2}}+\left[\sigma_2^2+\sigma_4^2\right]^{\frac{1}{2}}}\right) \tag{20}$$

$$\Delta\phi_{\text{err}} = \angle(\sigma_2 + j\sigma_4) - \angle(\sigma_1 + j\sigma_3) - \frac{\pi}{2} \tag{21}$$

where $\angle$ stands for the phase of a given complex number, in radians. Equation (20) measures the similarity in the magnitude of the output vectors $([i_I'(t_k), i_Q'(t_k)])$ in the I/Q plane when a perfectly in-phase $([i_I(t_k), i_Q(t_k)] = [1, 0])$ and quadrature signal $([i_I(t_k), i_Q(t_k)] = [0, 1]])$ is present at the input of the hybrid. Equation (21) quantifies the deviation of the angle between these two output vectors with respect to an ideal quadrature system $(\pi/2)$.

The system level simulation procedure can be described as follows. For every possible field transmission matrix computed in Section 2, a 2×2 real-valued matrix (Σ) is computed using (16)–(19). From this matrix, both figures of merit ($\text{CMRR}_{I/Q}$ and $\Delta\phi_{\text{err}}$) are calculated. Secondly, a Monte Carlo system simulation is run in Matlab so as to determine the hybrid-induced penalty with respect to an ideal system, whose BER is given by (8). The penalty is computed at a BER of 10^{-3}, which is considered a typical value in order to ensure correct operation of forward error correction (FEC) codes. Each Monte Carlo simulation involved the transmission of 2^{24} symbols, guaranteeing a penalty resolution of $\simeq \pm 0.08$ dB with a 95% probability [27]. $\Delta f_{3\text{ dB}}$ is set to 50 GHz, whereas B_{res} is set to 12.5 GHz (0.1 nm), which agrees with the OSNR's resolution bandwidth employed in previous experimental demonstrations [5], [28].

In Fig. 6, both electrical CMRR and phase error are plotted for comparison using the *dimensional stacking* technique. Additional post-processed results are shown in Fig. 7, following the same worst case methodology as described in Section 2. Penalty figures are shown in Fig. 8. From them, some interesting conclusions can be drawn. First of all, note how the operating bandwidth is considerably increased in the electrical domain. For example, the worst case optical CMRR in Section 2 (CMRR In-2, I and Q) achieves a 20-nm bandwidth (1537.5–1557.5 nm), whereas the electrical CMRR (CMRR I/Q) reaches up to 45 nm (1530–1575 nm). On the other hand, the worst case optical phase error $(\phi_1 - \phi_4 + 180^\circ)$ in Section 2 only meets specifications over a 10-nm bandwidth (1540–1550 nm), as opposite to the 37.5 nm (1532.5–1570 nm) provided by the electrical phase error $(\Delta\phi_{\text{err}})$. Although device dimensions are different, our electrical domain results are similar to those experimentally provided in [10] and [21], where the performance of a 4×4 MMI-based 90° optical hybrid manufactured using the same technology is reported.

The resulting improvements in performance can be put down to the mutual cancellation of optical imbalance between the LO and signal branches. As it has been previously mentioned, if the transmission coefficients in (14) vary in such a way that their product is unchanged, no net imbalance occurs. Our simulations indicate that this self-cancelling effect is indeed achieved when

using MMI-based structures. This behavior can in turn be related to the inherent robustness of MMIs, whose imaging properties rely on the difference in effective indexes between propagating modes. Since their propagation constants are similarly affected by the tolerances of the process, their difference remains almost the same. Thus, MMI-based structures are inherently resilient against manufacturing deviations and boast a wide operation bandwidth. As a result, any optical hybrid based on 4 $\times$ 4-MMIs will most likely exhibit this kind of self-compensating effect, independently of the technology. However, it might not be necessarily true for other types of hybrids, such as those based on directional couplers and waveguide phase shifters [4] or interleaved-chirped AWGs [5], which would require additional investigation. Note also that this improvement is independent of the relative power between the LO and the signal since it only depends on the optical response of the hybrid (that is, the relative phases and amplitudes between the different input and output ports).

By having a further look at both Figs. 7 and 8, it is clear that a strong correlation exists between our proposed system level figures of merit and the imbalance-induced penalty. In fact, power penalty remains lower than 1 dB for approximately 40 nm (1530–1570 nm), which is close to the bandwidth of both CMRR I/Q and $\Delta\phi_{\text{err}}$ as defined by OIF specifications ($\leq$ 45 nm and $\leq$ 37.5 nm, respectively). As a consequence, electrical figures of merit can provide designers with a more accurate estimation of operation bandwidth when power penalty is of major concern. Besides, the associated improvement translates into a higher fabrication yield and lower manufacturing costs, relaxing constraints on the foundry process. Our results predict that a worst case operation bandwidth of $\simeq$40 nm showing penalties lower than 1 dB is possible with realistic state-of-the-art manufacturing technologies, even if the worst case scenario is considered. Not only that, low penalties ($\leq$ 0.25 dB) are achieved along the C band, thus guaranteeing high BER performance for all devices manufactured under the same platform.

4. Conclusion

In this paper, a systematic numerical evaluation of the impact that manufacturing deviations have on the performance of a 90° optical hybrid has been performed, including their impact at both the physical and system levels. Multiple combinations of MMI's width, thickness, and core refractive index have been simultaneously swept over the C and L bands, taking into account real measured values from a state-of-the-art integration platform. On one hand, our results indicate that big differences in operation bandwidth result between ideal and worst case scenarios, which points out to the need of taking these deviations into account when estimating bandwidth via numerical simulations. On the other hand, system level results show that commonly used figures of merit, such as CMRRs and phase errors in the optical domain, do not provide a direct measure of the operation bandwidth when power penalty is to be considered. Instead, their electrical counterparts need to be used, which can be easily calculated from physical level simulations. Less than 1 dB of power penalty ($@\text{BER} = 10^{-3}$) is predicted for about 40 nm (1530–1570 nm) in the worst case scenario and $\leq$ 0.25 dB over the full C band. This contrasts with the fact that only 10 nm are achieved if optical CMRRs and phase errors are compared against well-known specifications [19]. These results, together with future advancements in fabrication technologies, further confirm the great potential of 4 $\times$ 4 MMI-based 90° optical hybrids as future ultra-wide bandwidth, low imbalance devices for integrated coherent receivers.

Acknowledgment

The authors are also grateful to the EuroPIC consortium (FP7 funded programme NMP 228839-2) for access to the design manual and design toolkit of the generic InP fab.

References

[1] M. Seimetz, *High-Order Modulation for Optical Fiber Transmission*. New York, NY, USA: Springer-Verlag, 2009.
[2] R. Nagarajan, M. Kato, D. Lambert, P. Evans, S. Corzine, V. Lal, J. Rahn, A. Nilsson, M. Fisher, M. Kuntz, J. Pleumeekers, A. Dentai, H.-S. Tsai, D. Krause, H. Sun, K.-T. Wu, M. Ziari, T. Butrie, M. Reffle, M. Mitchell, F. Kish,

and D. Welch, "Terabit/s class InP photonic integrated circuits," *Semicond. Sci. Technol.*, vol. 27, no. 9, p. 094003, Sep. 2012.
[3] J. T. Rahn, S. Kumar, M. Mitchell, R. Malendevich, H. Sun, K.-T. Wu, P. Mertz, K. Croussore, H. Wang, M. Kato, V. Lal, P. Evans, D. Lambert, H.-S. Tsai, P. Samra, B. Taylor, A. Nilsson, S. Grubb, R. Nagarajan, F. Kish, and D. Welch, "250 Gb/s real-time PIC-based super-channel transmission over a gridless 6000 km terrestrial link," in *Proc. Nat. Fiber Optic Eng. Conf.*, 2012, pp. 1–3.
[4] M. Seimetz and C.-M. Weinert, "Options, feasibility, and availability of 2 × 4 90° hybrids for coherent optical systems," *J. Lightw. Technol.*, vol. 24, no. 3, pp. 1317–1322, Mar. 2006.
[5] C. Doerr, L. Zhang, and P. Winzer, "Monolithic InP multiwavelength coherent receiver using a chirped arrayed waveguide grating," *J. Lightw. Technol.*, vol. 29, no. 4, pp. 536–541, Feb. 2011.
[6] R. Halir, G. Roelkens, A. Ortega-Moñux, and J. G. Wangüemert-Pérez, "High-performance 90° hybrid based on a Silicon-on-insulator multimode interference coupler," *Opt. Lett.*, vol. 36, no. 2, pp. 178–180, Jan. 2011.
[7] R. Kunkel, H.-G. Bach, D. Hoffmann, C. Weinert, I. Molina-Fernandez, and R. Halir, "First monolithic InP-based 90° hybrid OEIC comprising balanced detectors for 100GE coherent frontends," in *Proc. IEEE Int. Conf. Indium Phosphide Relat. Mater.*, May 2009, pp. 167–170.
[8] S.-H. Jeong and K. Morito, "Novel optical 90° hybrid consisting of a paired interference based 2 × 4 MMI coupler, a phase shifter and a 2 × 2 MMI coupler," *J. Lightw. Technol.*, vol. 28, no. 9, pp. 1323–1331, May 2010.
[9] S.-H. Jeong and K. Morito, "Compact optical 90° hybrid employing a tapered 2× 4 MMI coupler serially connected by a 2× 2 MMI coupler," *Opt. Exp.*, vol. 18, no. 5, pp. 4275–4288, Mar. 2010.
[10] H.-G. Bach, A. Matiss, C. Leonhardt, R. Kunkel, D. Schmidt, M. Schell, and A. Umbach, "Monolithic 90° hybrid with balanced PIN photodiodes for 100 Gbit/s PM-QPSK receiver applications," in *Proc. Opt. Fiber Commun. Conf.*, Mar. 2009, pp. 1–3.
[11] M. Boudreau, M. Poirier, G. Yoffe, and B. Pezeshki, "An integrated InP-based coherent receiver for 40 and 100 Gb/sec telecommunications systems," in *Proc. Opt. Fiber Commun. Conf.*, Mar. 2009, pp. 1–3.
[12] L. Zimmermann, K. Voigt, G. Winzer, K. Petermann, and C. Weinert, "C-band optical 90° hybrids based on silicon-on-insulator 4 × 4 waveguide couplers," *IEEE Photon. Technol. Lett.*, vol. 21, no. 3, pp. 143–145, Feb. 2009.
[13] K. Voigt, L. Zimmermann, G. Winzer, H. Tian, B. Tillack, and K. Petermann, "C-band optical 90° hybrids in silicon nanowaveguide technology," *IEEE Photon. Technol. Lett.*, vol. 23, no. 23, pp. 1769–1771, Dec. 2011.
[14] R. Halir, I. Molina-Fernandez, A. Ortega-Monux, J. Wanguemert-Perez, D.-X. Xu, P. Cheben, and S. Janz, "A design procedure for high-performance, rib-waveguide-based multimode interference couplers in silicon-on-insulator," *IEEE Photon. Technol. Lett.*, vol. 26, no. 16, pp. 2928–2936, Aug. 2008.
[15] I. Fatadin, S. Savory, and D. Ives, "Compensation of quadrature imbalance in an optical QPSK coherent receiver," *IEEE Photon. Technol. Lett.*, vol. 20, no. 20, pp. 1733–1735, Oct. 2008.
[16] C. Petrou, A. Vgenis, I. Roudas, and L. Raptis, "Quadrature imbalance compensation for PDM QPSK coherent optical systems," *IEEE Photon. Technol. Lett.*, vol. 21, no. 24, pp. 1876–1878, Dec. 2009.
[17] P. Besse, M. Bachmann, H. Melchior, L. Soldano, and M. Smit, "Optical bandwidth and fabrication tolerances of multimode interference couplers," *J. Lightw. Technol.*, vol. 12, no. 6, pp. 1004–1009, Jun. 1994.
[18] J. LeBlanc, M. Ward, and N. Wittels, "Exploring n-dimensional databases," in *Proc. 1st IEEE Conf. Visual.*, Oct. 1990, pp. 230–237.
[19] "Implementation Agreement for Integrated Dual Polarization Intradyne Coherent Receivers," in *Optical Internetworking Forum Std.*, OIF-DPC-RX-01.1, Sep. 2011.
[20] M. Bachmann, P. A. Besse, and H. Melchior, "Overlapping-image multimode interference couplers with a reduced number of self-images for uniform and nonuniform power splitting," *Appl. Opt.*, vol. 34, no. 30, pp. 6898–6910, Oct. 1995.
[21] R.-Y. Zhang, K. Janiak, H.-G. Bach, R. Kunkel, A. Seeger, S. Schubert, M. Schell, A. Matiss, and A. Umbach, "Performance of InP-based 90°-hybrids QPSK receivers within C-band," in *Proc. 23rd Int. Conf. Indium Phosphide Relat. Mater.*, May 2011, pp. 1–3.
[22] E. Ip, A. P. T. Lau, D. J. F. Barros, and J. M. Kahn, "Coherent detection in optical fiber systems," *Opt. Exp.*, vol. 16, no. 2, pp. 753–791, Jan. 2008.
[23] S. Betti, G. Marchis, and E. Iannone, *Coherent Optical Communication Systems*. Hoboken, NJ, USA: Wiley, 1995.
[24] T. Strasser and J. Wagener, "Wavelength-selective switches for ROADM applications," *IEEE J. Sel. Topics Quantum Electron.*, vol. 16, no. 5, pp. 1150–1157, Sep./Oct. 2010.
[25] G. Goldfarb and G. Li, "BER estimation of QPSK homodyne detection with carrier phase estimation using digital signal processing," *Opt. Exp.*, vol. 14, no. 18, pp. 8043–8053, Sep. 2006.
[26] M. Simon, "On the bit-error probability of differentially encoded QPSK and offset QPSK in the presence of carrier synchronization," *IEEE Trans. Commun.*, vol. 54, no. 5, pp. 806–812, May 2006.
[27] M. Jeruchim, "Techniques for estimating the bit error rate in the simulation of digital communication systems," *IEEE J. Sel. Areas Commun.*, vol. SAC-2, no. 1, pp. 153–170, Jan. 1984.
[28] C. Doerr, L. Buhl, Y. Baeyens, R. Aroca, S. Chandrasekhar, X. Liu, L. Chen, and Y.-K. Chen, "Packaged monolithic silicon 112-Gb/s coherent receiver," *IEEE Photon. Technol. Lett.*, vol. 23, no. 12, pp. 762–764, Jun. 2011.